communications biology

A Nature Portfolio journal

Article

https://doi.org/10.1038/s42003-026-09637-4

Periodic confined cell migration drives partially reversible chromatin reorganization in cancer cell lines

Maria del Valle Blazquez-Romero [1,2,3], Marco Mendivil-Carboni [4,5], Maria Sarasquete-Martinez[3], Alejandro Sainz-Agost[6,7], Fernando Falo [6,7], Marco De Corato [1,3] ✉ & Maria Jose Gomez-Benito [2,3] ✉

Cells throughout physiological and pathological contexts are exposed to a broad spectrum of mechanical stimuli, triggering extensive nuclear deformation and chromatin remodeling. These mechanical cues drive the cell to dynamically adapt through coordinated structural, epigenetic, and biochemical mechanisms to withstand mechanical stress while protecting genomic integrity. However, whether such cellular adaptations are reversible or result in persistent alterations remains unresolved. In cancer metastasis, addressing this issue is critical: confined migration through narrow pores prompts chromatin condensation with heterochromatin enrichment, yet cancer cells must preserve their oncogenic potential while preparing for future deformations. Therefore, the ability of these cells to reconcile reversible chromatin remodeling and mechanical memory could be key to metastatic resilience. Here, using a custom-designed microfluidic device to monitor single-cell chromatin reorganization, we show confined migration induces partially-reversible chromatin condensation: total highly-condensed chromatin content is recovered after deformation, but the distribution of condensed chromatin clusters remains altered. Our findings highlight this duality of chromatin condensation as both a short-term adaptive response and a mechanical memory strategy, which could potentially contribute to address cancer invasiveness.

Cell migration is a chemically and mechanically coordinated process that plays a fundamental role in multiple biological phenomena, from major developmental stages to wound healing and immune response in adults. Its relevance extends beyond its physiological function to be a pivotal factor in various pathological processes, particularly in cancer metastasis[1,2].

During metastatic migration in vivo, cancer cells adapt to heterogeneous microenvironments to invade other tissues as they encounter physical barriers, including confining pores or tight channel-like tracks[3–5]. Consequently, cancer cells are frequently subjected to confined cell migration when they squeeze through narrow gaps, often smaller than their nuclear diameter[6]. Besides confined migration, cells experience other types of mechanical stimuli such as fluid shear stress[7], substrate stiffness[8] and topography[9,10], stretching[11] or cell compression[12,13]. As a mechanosensitive element, the nucleus responds and propagates these external mechanical cues from the cytoskeleton to the DNA[8,14]. This signaling cascade can activate molecular pathways on the scale of minutes to hours[15,16], and it can also directly modify the internal environment of the nucleus over much faster timescales[17,18].

The nucleus contains the DNA arranged with packaging proteins to form chromatin, where DNA chains wrap around histone protein complexes[19,20]. Gene expression depends on the accessibility of DNA chains packed in these dense structures. Therefore, chromatin transitions dynamically between decondensed and condensed states to regulate gene accessibility, resulting in two chromatin phases: euchromatin and heterochromatin. Euchromatin domains are loosely packed, hence favoring DNA accessibility and acquiring a transcriptionally active role in gene expression. On the contrary, heterochromatin domains present a dense, tightly packed

[1]Department of Science and Technology of Materials and Fluids, Fluid Dynamics Technology Group (TFD), Universidad de Zaragoza, Zaragoza, Spain. [2]Department of Mechanical Engineering, Multiscale in Mechanical and Biological Engineering (M2BE), Universidad de Zaragoza, Zaragoza, Spain. [3]Aragon Institute of Engineering Research (I3A), Zaragoza, Spain. [4]Department of Structure of Matter, Thermal Physics and Electronics, Universidad Complutense de Madrid, Madrid, Spain. [5]Interdisciplinary Group on Complex Systems (GISC), Universidad Complutense de Madrid, Madrid, Spain. [6]Department of Condensed Matter Physics, Universidad de Zaragoza, Zaragoza, Spain. [7]Institute for Biocomputation and Physics of Complex Systems (BIFI), Universidad de Zaragoza, Zaragoza, Spain. ✉e-mail: mdecorato@unizar.es; gomezmj@unizar.es

configuration which is generally associated with low DNA accessibility and gene silencing[8,19,21].

The coexistence of these two distinct chromatin phases is likely the result of phase separation driven by thermodynamic potentials due to attractive interactions between heterochromatin regions[22], like in the case of nuclear protein condensates[23], and active nonequilibrium processes[24–26].

Chromatin has emerged as a crucial determinant of nuclear mechanics, playing a key role as a dynamic mechanoresponsive element resisting external loads[19,21,27–29]. Compressive deformations applied to the nucleus promote chromatin condensation by increasing the degree of methylation to form heterochromatin-rich regions[12,13,30]. They have also been linked to alterations in the dynamic behavior of nuclear condensates, for example, a reduction in the number and size of HP1α condensates, which are known to interact with heterochromatin regions[31]. Conversely, experiments applying stretch deformations to nuclei induce loss of condensed regions with decreased levels of histone methylation[11]. Interestingly, recent observations suggest that there is a chemo-mechanical feedback loop between nuclear mechanics and chromatin organization[21,32,33]. Mechanical forces alter chromatin architecture, which can enable or modulate histone modifications that influence gene expression and cell fate[34,35]. These epigenetic changes simultaneously alter nuclear properties, including stiffness, to adjust nuclear deformability while protecting genomic integrity[11,27,36,37]. Ultimately, the modification of nuclear properties to adapt to the mechanical context closes the loop by instilling a mechanical memory that facilitates subsequent nuclear deformations[12,28,29].

Nevertheless, the potential reversibility of these chromatin alterations remains debated. Compressive loading experiments reveal reversible chromatin condensation and transient heterochromatin enrichment, yet these effects are limited to short-term loading (less than one hour)[12,13]. On the contrary, long-term and repetitive loading show persistent structural and expression changes acting as mechanical memory to the cells[12]. Similarly, confined migration triggers the formation of non-reversible heterochromatin markers (e.g., H3K9me^3, H3K27me^3) that consistently endure after deformation[30].

Whether these chromatin alterations reset post-deformation or persist as a mechanical memory strategy is crucial in metastasis spreading. Cancer cells require reversible chromatin condensation to preserve their overly active malignancy-driving gene expression while concurrently undergoing long-term modifications to prepare for future deformations.

Despite substantial progress, mechanisms coupling chromatin condensation to nuclear adaptability upon deformations, and the spatio-temporal regulation of reversible versus persistent chromatin condensation, are still unresolved. Addressing these questions would advance our understanding of the dynamic interplay between mechanical forces and chromatin remodeling during metastasis and, potentially, support innovative mechanotherapy strategies aiming to control tumor invasion[38].

Here, we designed a microfluidic device consisting of repetitive confining and non-confining regions to monitor single-cell chromatin dynamics. We find that chromatin condensation levels reversibly increase upon nuclear deformation through confinement, while condensed chromatin clusters exhibited an altered size and number distribution post-deformation. These observations point to an incomplete chromatin relaxation, consequently, partially reversible chromatin condensation. Based on our numerical simulations, the deformation and the attractive interactions between heterochromatin domains could explain chromatin reorganization. Taken together, our findings suggest that partially-reversible chromatin condensation acts as an adaptive mechanism in cancer cells to mediate both gene expression regulation and persistent mechanical memory, which reveals the inherent duality in chromatin dynamics.

Results

Nuclear area minimally reduces upon nucleus deformation through microfluidic constriction

We developed a high-throughput approach for single-cell analysis based on high-resolution real-time imaging of cancer cells with metastatic potential migrating through confining channels in a microfluidic device. These cells were transfected to express human histone H2B, one of the core proteins in DNA packaging, labeled with Green Fluorescent Protein (GFP). Accordingly, the fluorescence intensity within the cell nucleus depends on the chromosome condensation state, hence, being a valuable tool to monitor DNA arrangement in vitro[39] (see Fig. 1a).

To address the potential reversibility of the nuclear alterations during confined migration, we implemented a microfluidic device in which the cells are guided through repetitive confinements. We propose an innovative design consisting of an array of parallel microchannels that alternate periodically between confining and non-confining regions with a constant height of 6 μm (Fig. 1b, c). The constrictions are defined by semicircular indentations of 4 μm in width at their narrowest point. This setup is intended to mimic the physiological constrictions that the cells encounter in vivo, particularly during intravasation and extravasation events[40].

Furthermore, the channels are engineered to confine the cells vertically throughout the migration path. Therefore, the cells inside the channels have a disc-like shape (Fig. 1e), establishing a direct correlation between the projected nucleus area (in the microscope images) and its volume. As a result of vertical confinement, cells exhibit a pseudo-2D deformation state, characterized by predominant deformation in the transverse plane (x-y plane, see Fig. 1c). The nature of this deformation suggests that chromatin movements in the vertical direction are unlikely to be influenced by the confinement. Consequently, these vertical fluctuations can be considered negligible, which supports our 2D imaging strategy. Focusing on a single optical slice of the nucleus minimizes cell phototoxicity and allows for shorter time-lapse intervals, which ultimately improves temporal resolution.

We were also curious to explore nuclear relaxation time after confinement. To motivate different migration speeds, our microfluidic chip incorporates two types of microchannels, characterized by longer or shorter non-confining regions (see Fig. 1c).

These chips were successfully developed, implemented, and proven to be effective in facilitating confined cell migration through multiple confinements (Fig. 1d and Supplementary Movie 1). The results for both long and short microchannels, in terms of the analyzed nuclear features, were strikingly similar. Indeed, the only observable difference was that more cells migrated through short channels and traveled longer distances than in long channels. Greater migration lengths in short channels could potentially be favored due to the proximity between adjacent constrictions and the prolonged confinement of the cytoplasm, which remains constricted even in non-confining regions. Consequently, for clarity, we present only the results for the short channels in this manuscript, while the results for the long channels are included in Supplementary Fig. 5.

We performed a thorough single-cell analysis, involving more than 100 migrating cells, to measure quantifiable morphological parameters for each nucleus to characterize its deformation (see Supplementary Fig. 3). The evolution of the parameters of interest was studied as a function of the position of the geometric center of the nucleus within the microchannel. The results for two representative cells are displayed in Fig. 2.

We were particularly interested in the evolution of the nucleus area through confinement. We identified two distinct behavioral patterns, one associated with fast cells and the other with slow cells. The former comprises cells that traverse the confinement in less than 40 minutes, whereas the latter includes cells requiring a longer time to complete the traversal.

Our analysis revealed that the nucleus area exhibits a sudden drop when entering the confinement for every cell, regardless of their migration speed. Following deformation, the nuclei recover their original area and, after overcoming multiple successive constrictions, the reduction of the area is similar in magnitude for each confinement, suggesting a completely reversible alteration of the nucleus area. In our experimental setup, the nuclear projected area is directly proportional to nuclear volume due to the vertical confinement imposed on the cells within the microchannels. Thus, these observations imply a reversible nuclear volume reduction, which has already described in the literature for confined cell migration[37,41]. We present two sample cells for the results of the single-cell analysis (Fig. 2), one slow

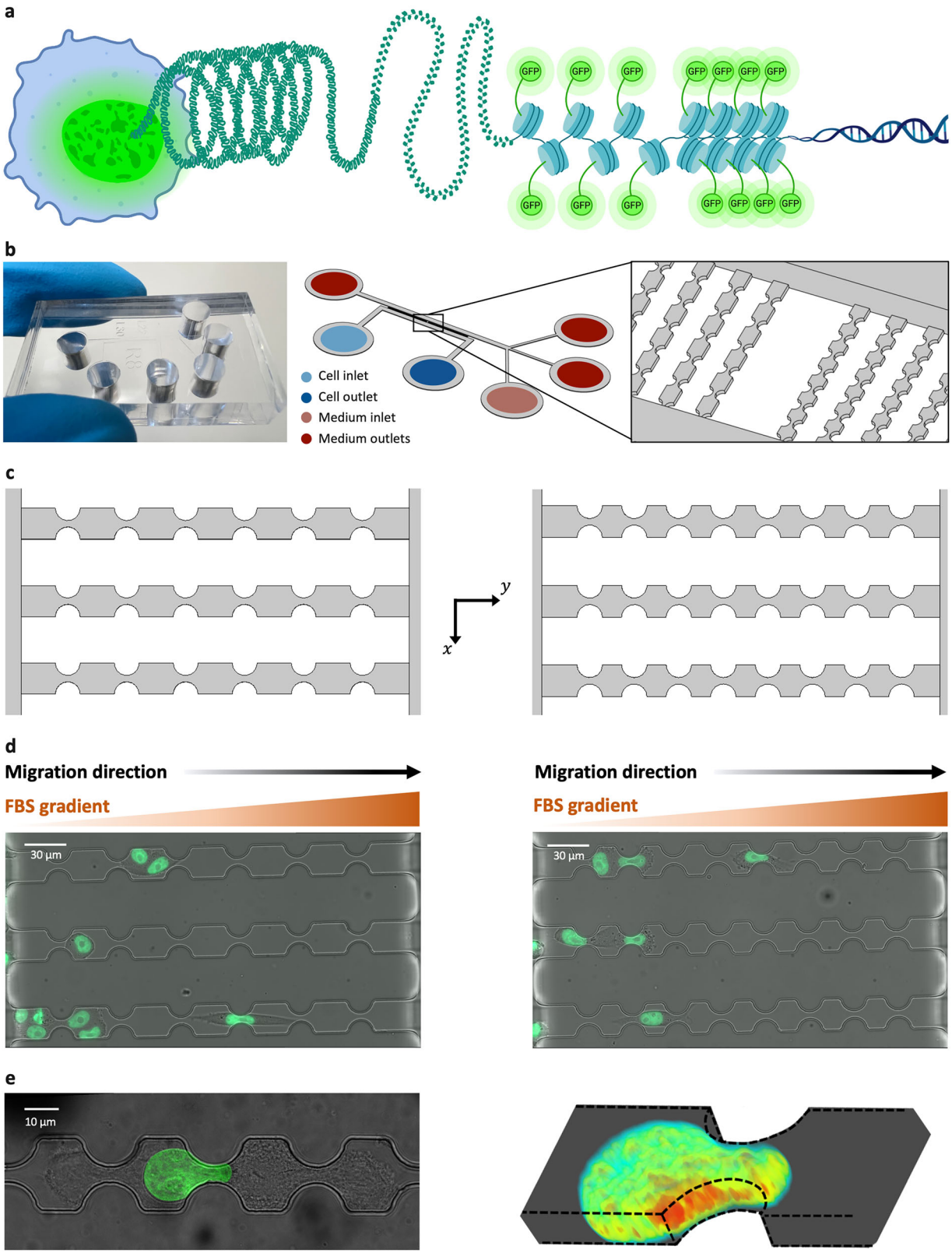

Fig. 1 | Overview of the experimental protocol and the design for our microfluidic device. a Fluorescence labeling of chromatin structure within the nucleus of the cell, representing different packaging levels of DNA and the fluorescent probes bonded to chromatin proteins, such that greater chromatin density corresponds to a higher fluorescence signal. Created with BioRender.com. **b** Three-dimensional view of the microfluidic device geometry consisting of an array of parallel microchannels of 250 μm long, which alternate between confining and non-confining regions. **c** Geometry detail for long channels (left) and for short channels (right) within the microfluidic device. Note that the channels through which the cells migrate are colored in gray. **d** Experimental example from optical microscopy for long channels (left) and short channels (right) where a chemical gradient (FBS in orange) was established to favor cell migration. **e** Confocal microscopy image of a cell migrating through a short channel (left) and its three-dimensional reconstruction, where the colormap represents GFP fluorescence intensity (right).

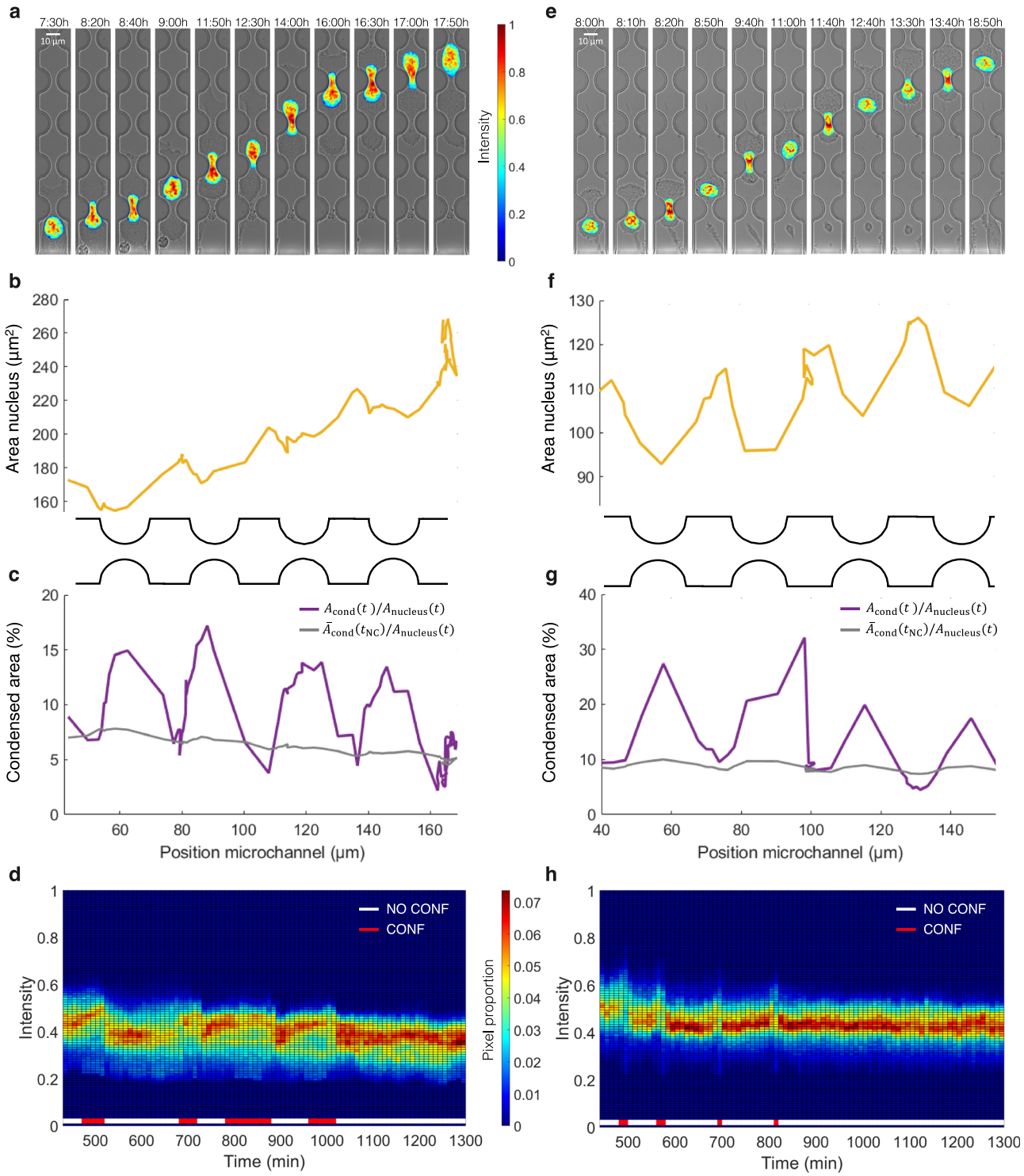

Fig. 2 | Single-cell analysis for A549-H2B-GFP cells migrating through periodic confinements in microfluidic devices. a–d Typical results for a representative slow migrating cell. **a** Time-lapse sequence displaying nuclear fluorescence intensity during migration through the microchannel. **b** Evolution of nuclear area plotted against the distance traveled within the channel. **c** Evolution of relative area of the segmented highly-condensed chromatin regions (in purple), i.e., overall condensed chromatin area ($A_{cond}(t)$) divided by the instantaneous nuclear area ($A_{nucleus}(t)$), and the mean condensed chromatin area during non-confinements ($\bar{A}_{cond}(t_{NC})$) divided by the instantaneous nuclear area, which represents the changes in chromatin condensation induced exclusively by changes in nuclear size (in gray). **d** Temporal evolution of the fluorescence intensity profile of the nucleus against time. **e–h** Similarly, typical results for a representative fast migrating cell. Upon deformation through each of the four confinements, both cells exhibit reversible nuclear shrinking, reversible increase in condensed chromatin area, and a distinctive transient dispersion in fluorescence intensity. Note that the increases during confinement in the gray curve for both cells do not explain the peaks in chromatin condensation in purple.

and one fast to traverse the constrictions. The slow cell (Fig. 2b) depicts a reduction of around 15 μm^2 in nuclear area for all confinements that were surpassed. Similarly, the fast cell (Fig. 2f) consistently decreases approximately 20 μm^2 its area.

Additionally, we noted that the nucleus area often exhibits not only a recovery of its original area but also a growing tendency after crossing a confinement. In fact, this event was observed in most cells except for a few cases displaying rapid migration. These particular cells migrated fast through both the constrictions and the non-confining segments of the channel. Therefore, cells that spend sufficient time in the non-confining regions, regardless of their speed to traverse the constrictions, show a noticeable increase in nucleus area with time. Nuclear growth is probably related to the progression of the cell cycle. The volume of the cell nucleus increases as the cell approaches mitosis, and slower cells have more time to progress through their cell cycle as they traverse the channels; hence, they frequently exhibit greater total nucleus growth than fast cells[20,42]. Consequently, fast cells lacking nuclear growth suggest that prolonged confinement leads to cell cycle arrest or delayed cell cycle progression as described by Bastianello et al.[43].

Owing to the viscoelastic behavior associated with the cell nucleus in the existing literature[28,41,44], we anticipated differences between slow and fast cells. Instead, the evolution of the area of the nucleus depicts a comparable pattern in both groups, characterized by a reversible reduction of the projected nuclear area upon confinement. This suggests that both cell groups migrate at a rate that is much slower than the viscoelastic relaxation time; hence, viscoelastic effects have already relaxed in our quasi-static images of the cell nucleus (10-minute frame interval). Despite nuclear shrinking being consistent among cells with different migration speeds, nuclear size did show a correlation with migration velocities (see Supplementary Fig. 4). As expected, the fastest cells are frequently characterized by smaller nuclear areas, and large cells are restricted to slower migration speeds through the microchannel[43]. Interestingly, migration speed broadens towards higher values during confinement, and there is a growing trend in migration velocities within non-confining regions as they are located further downstream, indicating that faster cells migrate deeper into the microchannel.

Total highly-condensed chromatin area increases reversibly in response to nuclear deformation

Next, we analyzed chromatin organization within the nucleus throughout the migration experiment. We quantified chromatin condensation levels using our segmentation algorithm that identifies highly fluorescent regions inside the nucleus of the cell (see Methods). Greater fluorescence is indicative of local histone accumulation and, hence, a more condensed chromatin structure[39]. Thus, these regions are referred to as highly-condensed chromatin regions or condensed chromatin clusters in this manuscript.

We computed the condensation level of the cell nucleus as the sum of every condensed chromatin cluster area over the total area of the nucleus, yielding the proportion of the nucleus occupied by highly-condensed regions. We find that there is a noticeable increase in the proportion of highly-condensed area whenever the cell migrates through a confinement. These shifts are observed for slow confined cell migration (Fig. 2c) and fast confined cell migration (Fig. 2g). In both cases, the evolution of the relative area for highly-condensed chromatin regions shows a prominent peak every time that the cell deforms through a confinement. Once the cell traverses the constriction, its condensation level returns nearly to its original value.

These spikes for highly-condensed chromatin area are often comparable in size, approximately increasing from 5 to 15% of the total nucleus area for the slow cell (Fig. 2c) and from 7 to 30% of the total nucleus area for the fast cell (Fig. 2g). Note that for fast cells (Fig. 2g), peaks in condensed chromatin area may exhibit greater variability due to the limited number of frames required for these cells to traverse the confinement. This reduced temporal resolution results in increased temporal variability, as the analysis may not capture a frame representing the cell at the same deformation state every time.

This trend for highly-condensed chromatin regions suggests that, upon cell deformation during confined migration, chromatin condensation level increases reversibly. After deformation, the nucleus recovers its basal chromatin condensation state, which generally lies around 5 to 10% of the total nucleus area. Note that the twofold to threefold increase in highly-condensed chromatin area cannot be explained by the decrease in nuclear area upon confinement. To represent the contribution of nuclear shrinking in the quantification of chromatin condensation, the gray line in Fig. 2c, g displays basal condensed chromatin content divided by the instantaneous area of the nucleus. Basal condensed chromatin represents the mean highly-condensed chromatin area of the nucleus, averaged over all non-confining regions (Entry, N1, N2…). Then, its evolution along the microchannel (gray curve) illustrates the changes in chromatin condensation induced by changes in nuclear area only. The notably limited growth during confinement does not explain the peaks in the segmentation of condensed chromatin area (in purple in Fig. 2c, g).

Fluorescent intensity distribution of the cell nucleus is altered upon deformation during confined migration

Subsequently, we sought to analyze changes in the fluorescence intensity profile of the cell nucleus. Initially, we investigated the evolution of the mean intensity and maximum intensity within the nucleus along the migration experiment for each cell.

The majority of the nuclei exhibited roughly constant values for mean and maximum intensities throughout the experiment (Supplementary Fig. 5c). Consequently, to capture rearrangements in chromatin content, we used a more robust analytical strategy to resolve spatial variations in fluorescence intensity rather than relying on global values. For each nucleus, we generated a colormap that represents the pixel proportion for the fluorescence intensity range (in the vertical axis) throughout every frame in the time-lapse migration experiment, such that each frame corresponds to a column in the horizontal axis (Fig. 2d, h).

Fluorescence intensity histograms over time often display large fluctuations in the pixel values during non-confining regions, which adds noise to the analysis (Fig. 2d, h). We observed that alterations in the fluorescence intensity profile upon the nucleus deforming through a confinement are highly heterogeneous among different cells. Yet, the fluorescence histograms depict a distinctive distribution in pixel proportion towards opposing ends of the intensity range whenever the cell traversed a confinement. Note that the intensity range is fairly constant during the analysis but, interestingly, the number of pixels with the highest and the lowest intensity levels increased simultaneously upon deformation (Fig. 2d, h). The shift observed for higher intensities is often stronger, displaying a characteristic rising tendency in the intensity profile at the frames in which the cell migrates through the confinement. This effect is visible in the results for the slow cell across all four confinements that the cell traverses (Fig. 2d). Despite the limited temporal resolution for fast cells, which frequently spend 10 to 20 minutes to traverse a constriction, this approach still captures the dispersion on pixel proportions during confined migration (Fig. 2h).

This distinctive pattern in the nuclear fluorescence intensity profile may reflect a dynamic spatial reorganization of chromatin architecture. A potential explanation is that nuclear deformation through confinement results in changes in the spatial distribution of chromatin, which form denser clusters in some regions while neighboring areas become less crowded, accounting for the simultaneous increase in higher and lower intensity pixels, respectively. This effect could also explain nearly constant mean and maximum intensity values (see Supplementary Fig. 5c).

Nuclear alterations in the projected area and chromatin condensation are consistent for cell populations across different cell lines

To confirm our findings, we complemented our single-cell observations with a population-level analysis. The cell population study accounts for intercellular heterogeneity and reveals meaningful trends in nuclear

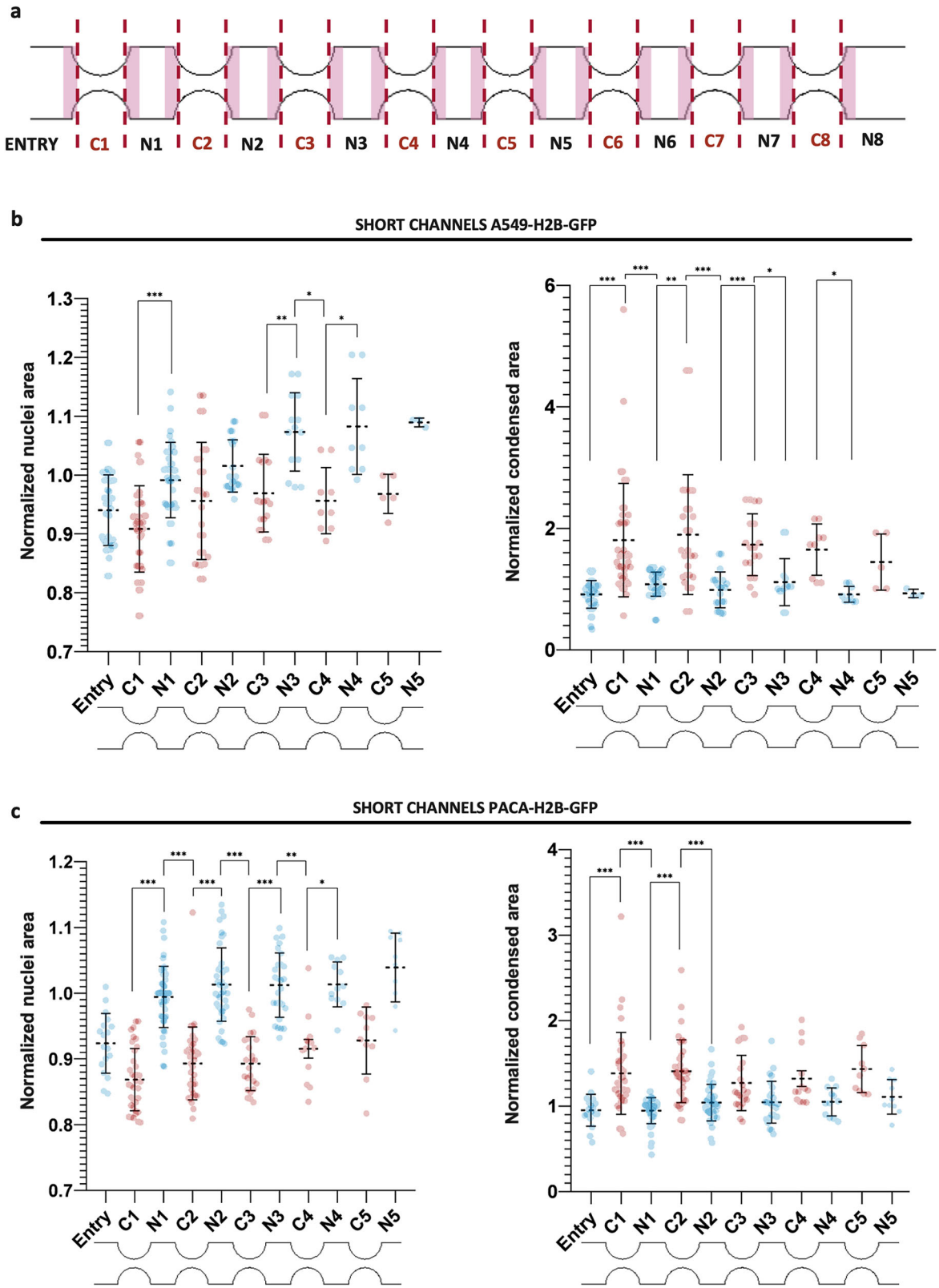

architecture while minimizing the influence of outliers and artifacts, providing statistically robust results.

The evolution of the nuclear area and the segmented relative area for highly-condensed chromatin regions were analyzed according to the nucleus position in the microchannel (Fig. 3). In the analysis, the column groups in the horizontal axis correspond to the different regions distinguished within the microchannel, confining (C1-C5) and non-confining regions (Entry and N1-N5) (Fig. 3a). Each dot in a column group corresponds to an individual cell, and it represents the average of the measured variable among every frame in which the geometric center of the cell lies within the specified region. Note that this data point is normalized with the mean of the variable among all non-confining regions (Entry, N1, N2…).

Fig. 3 | Distributions for the cell population analysis in short channels across two different cell types. a Diagram of the microchannel geometry, indicating the distinct regions distinguished for the analysis: non-confining regions shown in white (Entry and N1-N8), confining regions limited in red (C1-C8), and transition zones colored in pink, which are excluded from the analysis. **b** Distributions of the cell population analysis for cell migration through short channels in the microfluidic device of A549-H2B-GFP cells ($n = 42$). Each data point in a column corresponds to a single cell and represents the average among every frame in which the geometric center of the cell lies within the specified microchannel region, where C1-C5 represent the successive confining regions, and N1-N5 represent the non-confining regions following the entry (see microchannel representation under the horizontal axis). Note that the results for the confinements are colored in red, whereas those for unconfined cells are in blue. Left: Evolution of the normalized nuclei area shows a significant reversible decrease upon the deformation through confinement and a global growing trend over time. Right: Evolution of the normalized highly-condensed chromatin area depicts a strong increase for confining regions and a recovery of the basal highly-condensed area for non-confining regions. **c** Similarly, distributions for normalized nuclei area (left) and normalized highly-condensed chromatin area (right) of PACA-H2B-GFP cells, which consistently reveal an analogous pattern ($n = 65$). Bars show mean ± standard deviation. Kruskal-Wallis test with Dunn's post hoc test for multiple comparisons was performed. See Supplementary Data 1 for the significance results among every pair of groups, p-value: $p < 0.05$ (*), $p < 0.01$ (**), $p < 0.001$ (***).

In agreement with our single-cell findings, the evolution of nuclear area along the regions in the microchannels (Fig. 3b, left) shows that the mean for the normalized nuclei area under confining conditions is consistently lower than the mean in non-confining regions. Therefore, the nuclear area is significantly reduced during confined migration. In addition, our population-level results also reflect the growing trend in nuclear area that was identified during the single-cell analysis, note the statistically significant difference between the mean for the normalized nucleus area in the entry and in N4 (see Supplementary Data 1 for the p-value between these two groups). A lower number of cells reach the end of the microchannels; hence, the last regions adjacent to C5 are not considered statistically significant owing to the reduced number of data points.

The results for the normalized relative area of highly-condensed chromatin regions reveal that the mean for chromatin condensation level during every confining region is significantly higher than the mean for adjacent non-confining regions (Fig. 3b, right). Furthermore, we noted that the mean for every non-confining region is approximately one, i.e., a cell has a similar condensed area in every non-confining region (p-values between non-confining regions failed to meet the significance criterion, see Supplementary Data 1). This supports the idea of a basal chromatin condensation level. Nuclei stably recover their original condensation level after every constriction, proving the reversibility of global chromatin condensation in these confinement devices.

After validating our results through cell population analysis using an established lung cancer cell line, A549-H2B-GFP cells (Fig. 3b), we extended our study to include another cell line with metastatic potential, PACA-H2B-GFP (Fig. 3c), which was derived from a pediatric neuroblastoma tumor.

The results obtained with the second cell line agree with the patterns observed in our initial cell line, consistent across both single-cell (Supplementary Fig. 2) and population-level analyses (Fig. 3c). This reproducibility across different cell lines reduces the likelihood that the results are due to unique characteristics of a single cell line, and thus is biologically relevant for different cancer cells.

Average condensed chromatin content is restored while chromatin cluster distribution remains altered after confinement

Once we verified the statistical reliability of our findings across different cell lines, we delved into the time-dependent changes in individual highly-condensed chromatin clusters. Our results indicate that chromatin condensation during nuclear deformation through confinement is reversible since the original condensed chromatin content is recovered after traversing the constriction. However, to determine if chromatin condensation is fully reversible, we checked if the reorganization of condensed chromatin clusters relaxes to the original chromatin distribution after the deformation is removed. Other protein condensates have been seen to fuse during confined cell migration[13,18], hence, we wondered whether dense chromatin clusters (1) aggregate into larger domains via coalescence, (2) expand as individual units, or (3) form new clusters of highly-condensed chromatin.

To study the evolution of condensed chromatin clusters upon the nucleus deformation through confinement, we analyzed the distribution of the areas for individual condensed chromatin clusters and of the total cluster number per nucleus.

To provide a comprehensive overview of these condensed chromatin clusters dynamics, we generated region-specific histogram charts that aggregate the relative area across all chromatin clusters within each cell nucleus (cluster area over total nucleus area) appearing in every temporal frame where the cell center lies within the specific microchannel region. Therefore, each column in the histogram represents the normalized number of clusters of a relative area that appear among all nuclei and all time steps in the experiments for a specific region. Note that the histograms are normalized with the total number of counts; therefore, the vertical axis represents the probability for the cluster sizes in the horizontal axis. Similar distribution plots were calculated for the number of condensed chromatin clusters in every nucleus throughout the migration experiment. These charts allowed us to capture population-level trends rather than focusing solely on single-cell differences.

Previous research on intracellular condensates dynamics has demonstrated that protein condensates tend to follow an exponential distribution[45] whereas the volume for the nucleoli has been related to a power law distribution[46,47]. In our case, the histograms for PACA-H2B-GFP (Fig. 4b) and A549-H2B-GFP (Supplementary Fig. 6a) cells are similar for both cell types. We find a distinctive, roughly linear decay (in logarithmic scale) at the smallest cluster areas, which suggests an exponential size distribution for the area of condensed chromatin clusters. This trend has a steeper slope for non-confining regions; for confinements, we observe a gentler slope and a higher probability to find large condensed areas. Regardless, smaller areas are still more likely to be found than larger ones. After the constriction, the original condensed chromatin content is restored, yet the distribution does not relax to the initial one. Instead, some of the larger areas for condensed chromatin clusters, which did not appear in the previous non-confining chart, remained. This finding implies that, despite basal condensation levels being restored, the size distribution of highly-condensed chromatin regions within the nucleus is not fully recovered after chromatin reorganization upon nuclear deformation. To quantify how different the distributions are from one another, we computed the Wasserstein distances[48] (Supplementary Fig. 7a, left). This pairwise comparison leads to notably shorter distances when comparing regions of the same confining category, either confining or non-confining. Distributions for the same confinement state are more similar to each other and, hence, these results align with reversible chromatin condensation. However, it is noteworthy that the distance between the Entry and the remaining non-confining regions increases with the number of confinements traversed by the cells. Interestingly, when pairing a confining region with a non-confining one, the Wasserstein distance consistently decreases as the non-confining region is located further downstream in the microchannel. This implies that, as the cell overcomes more confinements, the distribution of chromatin cluster sizes in non-confining regions aligns more closely with those in confining regions. This trend supports our conclusion that cluster size distribution shifts towards larger values, characteristic of distributions during confinement, as the cancer cell migrates through successive constrictions.

Studying the distribution of cluster number allowed us to delve further into the condensation mechanism for chromatin domains. Prior to migration through confinement, most cells predominantly display 5–10 chromatin clusters (see Fig. 4c). Upon entering confinement, cells tend to

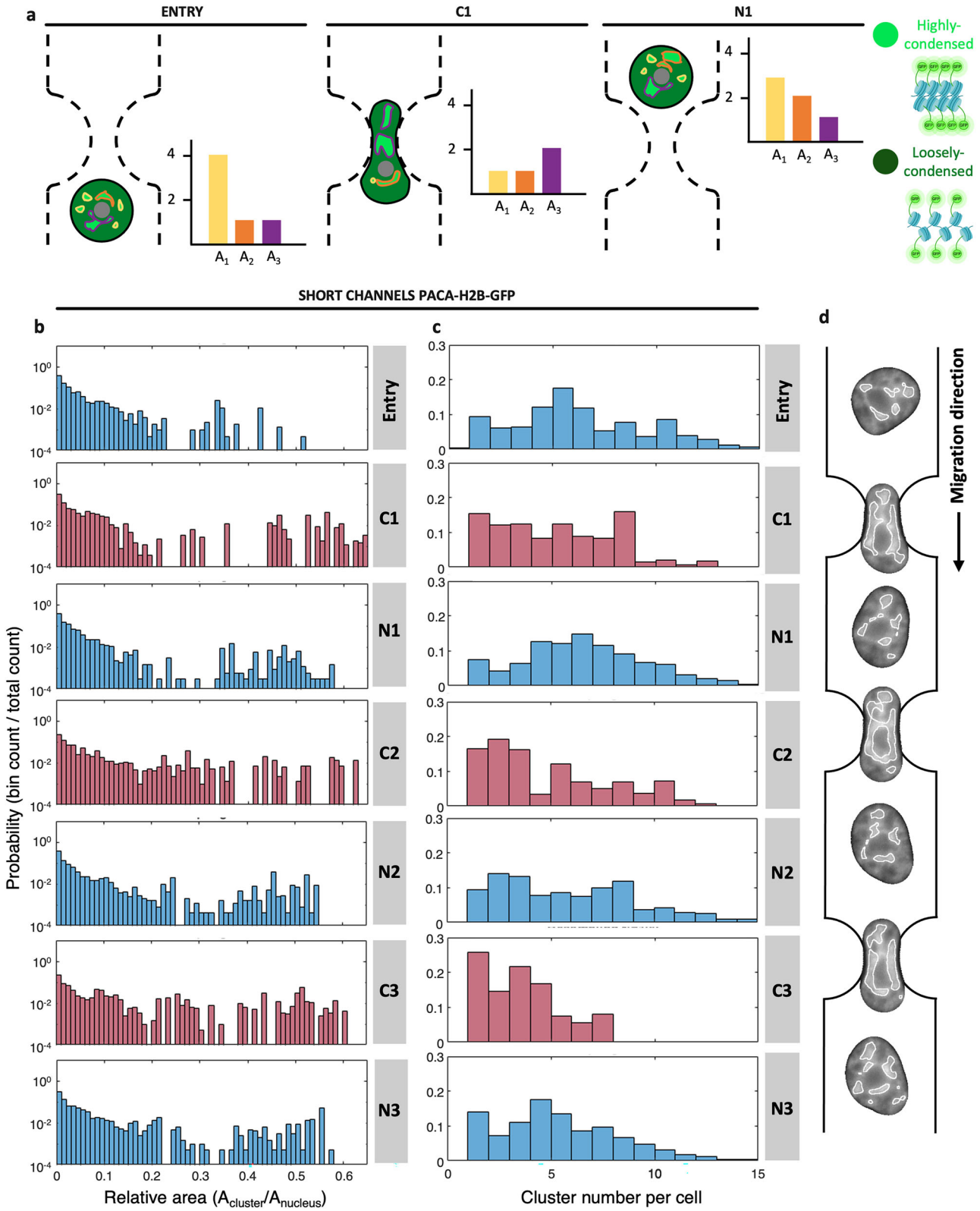

exhibit fewer clusters and, after exiting the constriction, the distribution broadens again towards higher cluster numbers. Nevertheless, as cells experience repetitive confinement cycles, lower cluster counts (typically 1-5 per cell) become progressively favored. This distribution pattern is consistent with chromatin cluster aggregation upon confined migration. During deformation, chromatin clusters come into proximity and tend to merge. They grow in size and, after confinement, some regions separate into individual clusters and revert to their initial state, whereas others remain fused, leading to an overall shift toward fewer but larger clusters. This explanation accounts for the simultaneous increase in cluster size and reduction in cluster number. Similarly to cluster size, the results for the pairwise comparison using Wasserstein distances (Supplementary Fig. 7a,

Fig. 4 | Distributions for the size and number of condensed chromatin clusters in PACA-H2B-GFP cells migrating through short microchannels. a Schematic of the quantification of the areas for condensed chromatin clusters. In the nucleus, before entering a constriction, there are mostly small areas (left), through a constriction, larger areas predominate (middle), and after a constriction, the cluster distribution is similar to the original, but middle-sized areas are favored (right). **b** Histograms to estimate the evolution of the size distribution for individual highly-condensed chromatin clusters in PACA-H2B-GFP cells (n=65). Histograms represent the normalized count (bin count over the total number of counts) for the relative area of individual highly-condensed chromatin areas, i.e., the area for each highly-condensed segmented region ($A_{cluster}$) over the total area of its nucleus ($A_{nucleus}$). From top to bottom, each graph corresponds to a different microchannel region, either non-confining (in red) or confining (in blue), and contains the relative area for every cluster in each nucleus during all frames in which the nucleus lies within the corresponding region. The counts for the condensed chromatin clusters in each cell are normalized to 100 data points to avoid misrepresenting cells that migrate faster through the microchannels. **c** Similarly, histograms were used to estimate the evolution of the distribution for the number of chromatin clusters per cell ($n = 65$). **d** Complementary illustration of the nucleus of a cell migrating through a microchannel with the segmentation of condensed chromatin clusters as an example to represent condensed chromatin cluster dynamics.

right) shows closer resemblance between distributions for regions of the same confining state and a trend towards shorter distance values when comparing confinements with non-confining regions further downstream the microchannel. Consequently, these results align with cluster size distributions to support that chromatin condensation during confined migration is only partially reversible for the $4 \times 6\ \mu m^2$ constrictions in our microfluidic devices.

Some proteins, such as Nesprin-2[49,50], have been shown to accumulate at the front of the cell during confined migration. To explore whether chromatin clusters accumulate preferentially at the front or the rear of the nucleus during successive confinements, we performed a cell population analysis considering the spatial distribution of these clusters. The distance between the center of mass, i.e., intensity weighted centroid of the nucleus, and the geometric center of the nucleus along the direction of the microchannel was used to estimate if the location where fluorescence intensity concentrates lies at the front or the rear of the nucleus. Nevertheless, the results were not consistent with a preferential accumulation of chromatin clusters on one side of the nucleus (see Supplementary Fig. 8). The distance from the center of mass to the geometric center along the microchannel direction is minimal and it does not exhibit a distinctive trend towards positive (accumulation at the front) or negative (accumulation at the rear) values.

Immunofluorescent assay matches highly-condensed chromatin areas to heterochromatin loci

Finally, we wondered whether the reorganization of condensed chromatin clusters during confined cell migration corresponds to heterochromatin loci. Therefore, we performed an immunofluorescent experiment using two well-established heterochromatin markers H3K27me^3 (cyan) and H3K9me^3 (magenta), which target two different chemical modifications on histone H3. Trimethylation of lysine 9 on histone H3 (H3K9me^3) is associated with constitutive heterochromatin, which is mostly located in centromeric and telomeric DNA regions, while trimethylation of lysine 27 on histone H3 (H3K27me^3) is associated with facultative heterochromatin, which is developmentally regulated.

Mapping these markers together with the GFP channel (green), to capture intrinsic GFP expression from the chromatin labeling on H2B, we could visualize the distribution of heterochromatin within chromatin content.

Firstly, we segmented the nucleus with our custom algorithm to identify highly-condensed chromatin regions over the fluorescent microscope images for both heterochromatin markers, and we found that the two markers mostly coincide with dense chromatin regions (bright regions) in the green channel. However, they do not appear in every condensed chromatin cluster that was originally segmented over the green channel. It is noteworthy that H3K9me^3 marker (magenta channel) is preferentially expressed in the nuclear periphery and around the nucleolus (Fig. 5), consistent with the literature in which H3K9me^3-rich domains anchor to the nuclear periphery to resist rupture[11].

To further unravel the relationship among condensed chromatin and heterochromatin markers, we computed the 2D correlation coefficient to evaluate the spatial correlation between the chromatin labeling (green) and each one of the heterochromatin markers. We obtained a remarkably high correlation coefficient for both arrangements, chromatin against H3K27me^3 (green against cyan) and chromatin against H3K9me^3 (green against magenta). Nevertheless, the former exhibits a significantly larger coefficient, which implies that fluorescent intensity distribution between chromatin and H3K27me^3 is particularly similar (Fig. 5b). This finding aligns with the developmental nature of facultative heterochromatin loci (H3K27me^3 marker), which have been shown to increase more than constitutive heterochromatin (H3K9me^3 marker) upon confined migration[30].

Chromatin computational model reproduces chromatin condensation observed in vitro

To understand the main mechanisms driving chromatin condensation during the translocation of the nucleus through a narrow constriction, we perform coarse-grained polymer simulations of the chromatin and the nucleus.

We describe chromatin using a single polymer chain made of $N = 60{,}000$ beads, each representing ~ 50000 base pairs. The polymer chain is divided into domains of heterochromatin and euchromatin, 64 beads long on average[51,52]. Simulations with chains of different domain sizes and with attractive interactions with the walls are explored in the Supplementary Note 1.

In previous experiments[7,13,30], chromatin condensation was associated with an increase in heterochromatin markers. By excluding biochemical reactions from our model, we can assess how much of the experimental observations can be explained through a purely physical reorganization of the chromatin. We tracked the evolution of chromatin concentration for a total simulation time corresponding to approximately 30 min of real time (Supplementary Movie 2). During this time, the shape of the nuclear boundary was deformed to mimic the cell migrating through a constriction (see Supplementary Note 1). To compute the local chromatin density, the positions of the beads inside the nucleus were projected onto the transverse plane, subdividing the area into equally sized pixels (with a side of 250 nm) and counting the number of beads in each one. Five snapshots of the resulting density maps obtained during the confined cell migration are shown in Fig. 6b.

Figure 6c represents the simulated distribution of chromatin density (ρ) in the nucleus over time. Similarly to Fig. 2d, h, each column in Fig. 6 corresponds to a particular instant of the simulation, and every row corresponds to a certain density value. We find a notable resemblance to the experimental observations (Fig. 2d, h) in the proportion of pixels with each density.

Before entering the constriction, the density of chromatin distribution within the nucleus is characterized by a main peak at a relatively low density. The beginning of nuclear confinement through the constriction takes place effectively at $t \approx 5$ min (second snapshot in Fig. 6d). The confinement of the nucleus drives chromatin reorganization, which results in a widening of the distribution of chromatin density. This implies a larger probability of finding both denser and looser regions than in the unconfined nucleus. Once the majority of the nucleus has traversed the constriction at $t \approx 18$ min (fourth snapshot in Fig. 6d), chromatin distribution partially relaxes back to its initial state. The recovery is not complete, since the peak in chromatin density shifts to smaller values compared to nuclei before the confinement (Fig. 6c). This implies that, by traversing the confinement, chromatin has concentrated in some regions, leaving others more depleted.

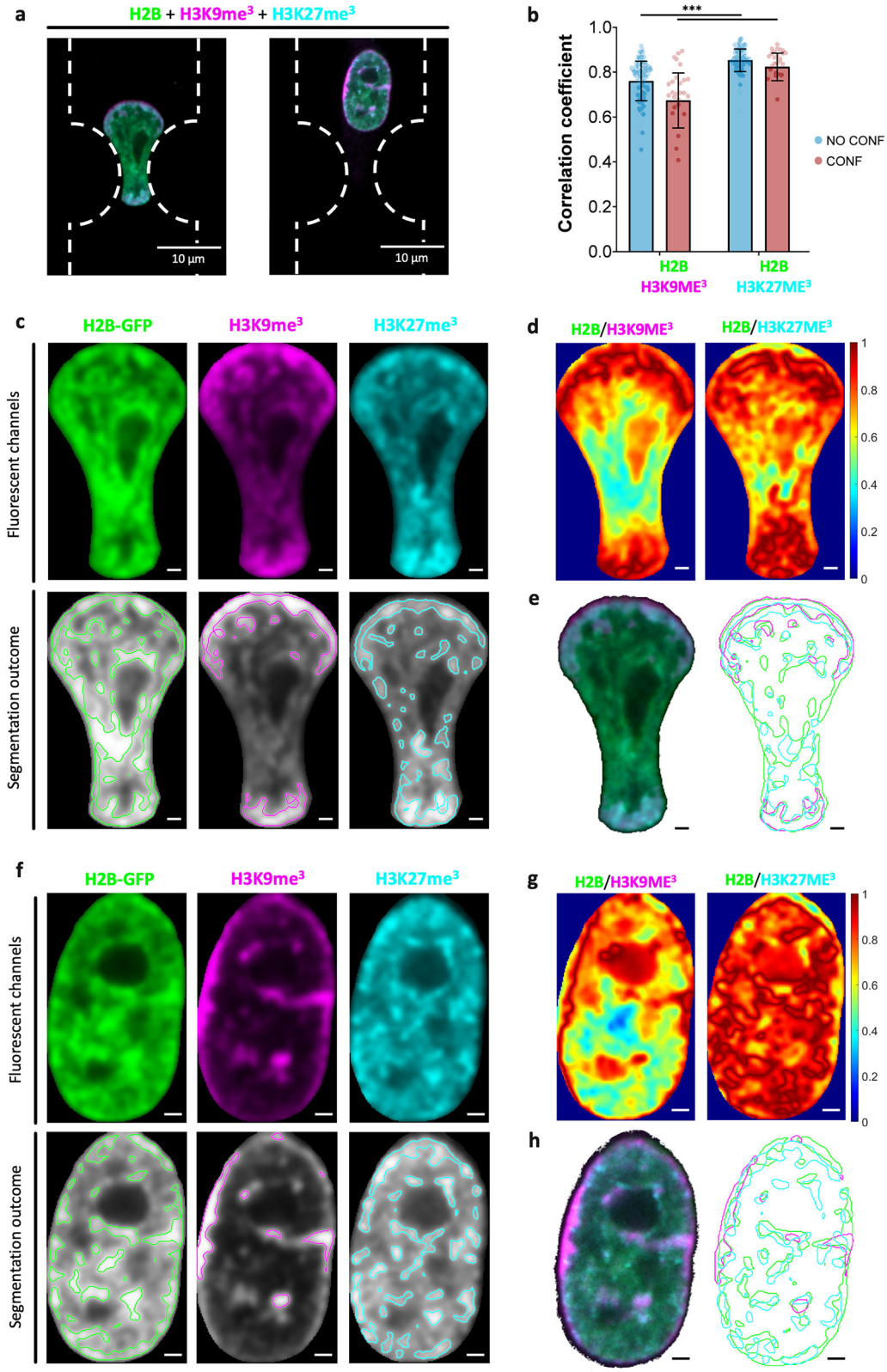

These observations are also reflected in the histograms for chromatin distribution in five particular snapshots of the simulation (Fig. 6e). The widening in chromatin distribution during confinement is appreciated by comparing the histograms for $t = 2$ min and $t = 9$ min. The height of the peak decreases, and the tail of the distribution rises. After confinement, corresponding to $t = 18$ min and $t = 28$ min, the density distribution is partially recovered ($\rho = 0.2$). The values of the density distribution for $\rho > 0.2$ are higher than for the unconstricted nucleus, suggesting a certain degree of irreversible behavior after confinement.

The simulation results agree with the experimental observations that chromatin reorganization due to confined cell migration is partially reversible. This supports our initial hypothesis that the origin of irreversibility in

Fig. 5 | Immunofluorescence assay for heterochromatin markers. a Merge of the fluorescent channels for a confined cell (left) and a non-confined cell (right): H2B-GFP (green), H3K9me^3-Alexa647 (magenta), and H3K27me^3-Alexa405 (cyan). Note that the dashed lines in white represent the microchannel's contour. **b** Bar chart representing the spatial correlation coefficient for chromatin distribution (green) against each heterochromatin marker (magenta and cyan), classified according to the confined state of the cell: confined (n=35) or non-confined (n=123). Error bars represent the standard deviation. Kruskal-Wallis test with Dunn's post hoc test for multiple comparisons was performed. **c** Normalized fluorescent images (top) and segmentation outcome (bottom) for each fluorescence channel in a confined cell. **d** Colormap representing the similarity between chromatin fluorescence image and each heterochromatin marker (H3K9me^3 and H3K27me^3). The colormap represents the inverse of the absolute difference between the pixels of each fluorescent channel image; then, one in the colormap corresponds to exactly the same pixel intensity in both images. **e** Merge of the fluorescent channels for a confined cell (left) and overlapping of the segmentation outcome for the three fluorescent channels (right). The correlation coefficients between H2B-GFP and the heterochromatin markers are 0.79 for H3K9me^3 and 0.90 for H3K27me^3. **f-h** Similarly, immunofluorescent analysis for a representative non-confined cell. The correlation coefficients between H2B-GFP and the heterochromatin markers are 0.64 for H3K9me^3 and 0.85 for H3K27me^3. Scale bars in the lower right corner correspond to 1 μm unless stated otherwise.

chromatin redistribution can be explained, qualitatively, using arguments based on polymer physics. Essentially, the nuclear deformation due to the constriction brings closer heterochromatin regions that were originally distant. Since these regions experience attractive interactions, they do not fully separate once the deformations are released. Nevertheless, our findings do not exclude other important contributions due to deformation-induced enzymatic modifications of histone marks. Previous experiments[11,13,30] have shown that these chemical reactions do take place experimentally, and they may well play an important role in determining the degree of chromatin reorganization irreversibility.

Discussion

In this work, we studied how periodic deformations applied to nuclei of metastatic cancer cells drive a net reorganization of chromatin. We used confined cell migration assays with periodic constrictions to apply controlled nuclear deformations. To specifically address the reversibility of nuclear alterations, we combine high-throughput real-time imaging of H2B-fluorescent cells at a single-cell resolution using a microfluidic device that features repetitive confining and non-confining regions. Unlike static compression and tensile models[11–13,17], which primarily study passive cellular responses, our microfluidic migration assay captures active cellular contribution to the dynamic and adaptive nuclear behavior[1,18,30,41], which is clinically relevant since it replicates the cyclic mechanical stress experienced during metastasis.

We found a significant increase in the highly-condensed chromatin area during nuclear migration through each confinement. The nuclear area occupied by condensed chromatin can reach up to threefold its value in a non-confined region, which cannot be explained by the small decrease in nuclear volume experienced during the confinement. Such overall increase of chromatin condensation is transitory, and the baseline levels are consistently recovered across the cell population once they traverse a constriction. Previous studies limit reversible chromatin condensation to short-term deformations (150 seconds to one hour) during dynamic loading[12], however, cells in our analysis exceeded this temporal threshold when migrating through a constriction and still show reversible effects (third confinement in Fig. 2b–d).

We then characterized the size distribution of highly-condensed chromatin clusters within different confined and non-confined sections of the microfluidic device. This approach yields more information than simply the average area of the nucleus occupied by condensed chromatin. We find that the distribution for small chromatin cluster sizes is not characterized by a power-law distribution as in the case of nucleoli[46,47] but by an exponential distribution (a linear decay at the beginning of our histograms in logarithmic scale), similar to that observed for intracellular protein condensates[45]. This suggests that a quench-then-coalesce mechanism might be responsible for the formation of small chromatin clusters. However, we consistently find probability peaks at higher cluster areas during confinement, which are absent in the case of protein condensates or nuclear speckles[45]. These peaks at larger cluster areas imply a growth in chromatin cluster area upon deformation. As cells traverse the channel, condensed chromatin clusters display an altered distribution after each constriction. Cluster size distribution shifts progressively towards larger areas as the cells migrate through repetitive confinements. Since the basal condensation level is recovered and the distributions for the number of clusters shift towards lower values, this implies that small clusters disappear to form larger clusters.

These observations, together with the single-cell analysis of the fluorescence intensity, suggest that deformation promotes the coalescence of smaller chromatin clusters, forming regions with higher chromatin density while leaving other regions more depleted. This is a different mechanism from that observed by Zhao et al.[18], where confined migration directly shifted the thermodynamic equilibrium phase separation of protein condensates and promoted the formation of new condensates. To support this hypothesis, we performed Brownian dynamics simulations of a model chromatin chain displaying self-attracting heterochromatin domains. The numerical results supported the notion that confined migration promotes the formation of larger chromatin condensates by bringing together small clusters, which then fuse.

The predominance of larger condensed chromatin clusters after confined migration might be related to the mechanical memory reported in the literature, where cells preserve structural changes to favor following deformation events[12,28,29]. The irreversible formation of heterochromatin loci was identified by Hsia et al.[30] after confined migration and can also be considered as a mechanical memory strategy of the cells[28]. Although their findings challenge reversible chromatin condensation, it is possible that, upon confinement, nuclear deformation causes chromatin to rearrange into denser regions without necessarily undergoing the chemical changes required to form heterochromatin. Thus, global chromatin condensation could have a reversible effect, while still preserving specific long-term heterochromatin loci from the confined migration as reported[30].

While our study provides compelling evidence that nuclear deformation under confinement is accompanied by adaptive chromatin rearrangements, further investigation is needed to elucidate how the deformation influences chromatin plasticity and its role in long-term epigenetic changes. To prioritize high temporal resolution while minimizing cell phototoxicity, we opted for a 2D imaging approach. This trade-off allowed for higher frame rates but limits a full three-dimensional characterization, which could be addressed in future studies with volumetric imaging. Despite this improved time-lapse interval (one frame every 10 minutes), our temporal resolution is not sufficient to capture rapid enzyme-mediated heterochromatin dynamics. Another limitation of our study arises from intercellular variability during the heterochromatin loci analysis. To identify heterochromatin domains within cell nuclei, cells were stained for two well-established heterochromatin markers, H3K9me3 and H3K27me3. However, the confining microchannels used in our experiments generate complex diffusion gradients of the staining reagents, leading to nonuniform marker distribution when multiple cells occupy the same channel. This effect introduces additional variability that constrains the precision of quantitative comparisons across nuclei. To compensate for diffusion-related variability, future analyses could include a complementary euchromatin marker (e.g., H3K9ac) to normalize the staining by computing the heterochromatin-to-euchromatin ratio in each cell. Addressing this limitation in the future could be interesting to study the evolution of persistent heterochromatin marks as the cells migrate further in the microchannel[30]. Future studies should aim at single-

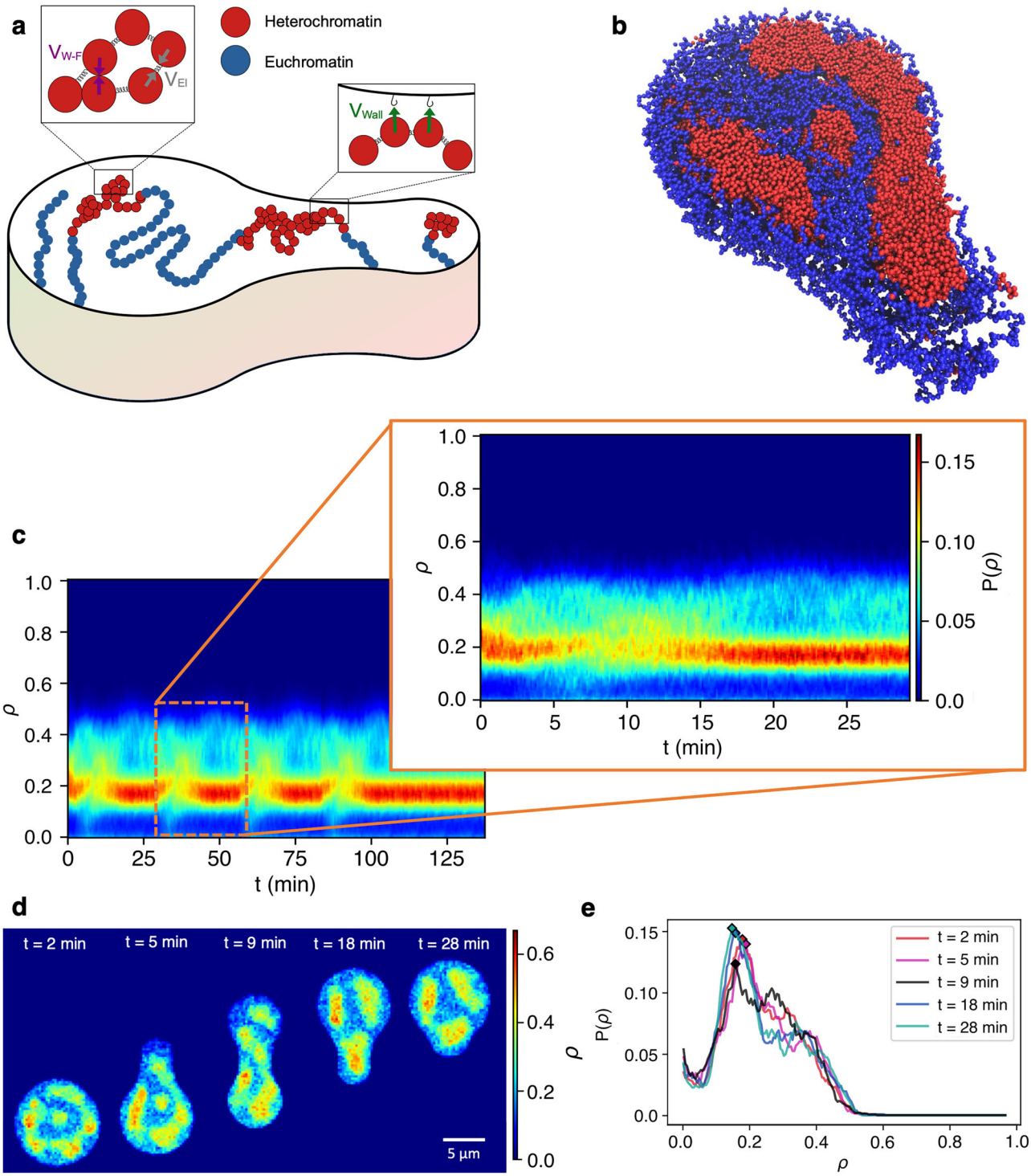

Fig. 6 | Polymer model to simulate chromatin dynamics during cell migration through a confinement. a Schematic of the chromatin model showing heterochromatin (in red), euchromatin (in blue), and elastic (V_{El}), Wang-Frenkel ($V_{W\text{-}F}$), and Wall (V_{Wall}) potentials in the insets of the figure. The geometry corresponds to a cell nucleus traversing a constriction within the microchannel. **b** Three-dimensional polymer representation of chromatin (heterochromatin beads in red and euchromatin beads in blue) within the nucleus as it enters a constriction (t ≈ 5 min). The figure shows the bottom region of the nucleus, sectioned at the mid-width plane. **c** Colormap depicting the evolution over time (horizontal axis) of the histogram of chromatin density (vertical axis) for a chromatin chain of $N = 60000$ and average domain size of 64 beads. The colormap corresponds to the pixel proportion with a particular density. The zoomed-in graph (right) represents the chromatin density profile for the simulation performed (30 minutes long), while the complete graph (left) displays a repetition of the simulation result (i.e., the zoomed-in graph) to reproduce the experimental time-scale for successive confinements in fast migrating cells. **d** Chromatin density distribution within the nucleus as it dynamically deforms to replicate the migration through a constriction in the microchannel. The time corresponding to each snapshot is shown at the top. **e** Histograms for chromatin density at different time points of the simulation, each corresponding to a column in the zoomed-in graph in (**c**). The diamond symbols indicate the maximum of each distribution.

cell sequencing to unravel how the deformation triggers specific chromatin states and epigenetic marks and should employ higher-resolution or real-time imaging techniques to capture finer-scale chromatin dynamics. Additionally, tracking daughter cells after mitosis could reveal interesting confinement-induced chromatin changes stably maintained beyond cell division, which may be related to potential metastatic regulators. Finally, validating these findings in more complex or in vivo models will be essential to completely uncover the implications of chromatin plasticity for metastatic potential and therapeutic targeting.

Methods

Design for microfluidic devices

We designed an innovative microfluidic device consisting of an array of parallel microchannels 250 μm long which alternate between confining and non-confining regions (see Fig. 1b and Supplementary Fig. 1). These microchannels have a height of 6 μm to confine vertically the cells into a two-dimensional disk-like shape without imposing excessive deformation to enable direct correlation between nuclear volume and the projected nuclear area in the microscope images. This setup is intended to guide cells through repetitive constrictions while enabling them to recover from the deformation to evaluate the potential short-term reversibility of nuclear alterations.

The confining regions within the microchannels are defined by semicircular indentations of 8 μm in radius, constricting the cross-section up to 4 μm at its narrowest point[40]. This pore size is sufficient to cause confinement-induced chromatin changes while preventing nuclear envelope rupture, common in constrictions smaller than $3.5 \times 6\ \mu m^2$ in cross-section[43]. For the non-confining regions, half of the microchannels are characterized by non-confining segments of 22 μm long, while the second half has 12 μm long segments between each confinement (Supplementary Fig. 1). This difference was designed to analyze the impact of different non-confining dimensions on the reversibility of the nuclear alterations.

Based on the state-of-the-art devices[5,30,53,54] and our experience with previous successful designs for confining microfluidic devices[3,55], the microchannels are orthogonally connected at each end to a seeding channel of 50 μm high, supplied by six loading ports of 4 mm in diameter. Loading ports are arranged as follows: Two communicating ports serve as the inlet and outlet for the cell seeding. The remaining four ports drain to the opposite seeding channel, and they are used to establish the optimal pressure difference that will direct cells to enter the microchannels (Supplementary Fig. 1).

Manufacturing of microfluidic devices for cell seeding

The microfabrication process for the microfluidic devices was performed as previously described by Shin et al.[56]. Briefly, SU-8 molds on silicon wafers with the desired microchannel geometries were manufactured using soft lithography in MicrofabSpace and Microscopy Characterization Facilities from the Institute for Bioengineering of Catalonia, IBEC, Barcelona, Spain. Polydimethylsiloxane (PDMS) (Sylgard-184, Dow, Midland, TX) at a 10:1 base-to-curing agent weight ratio was used to procure the mold replicas. Each microfluidic device in the resulting replica was trimmed individually in a rectangular shape using a blade, and the loading ports in each device were cored with a 4 mm biopsy punch (Miltex). Subsequently, they were sterilized in a two-step autoclave and, eventually, each microfluidic device was sealed to a sterile 24 × 40 mm glass coverslip (Rectangular Cover Glasses No.1, VWR) through plasma activation in the plasma cleaner (Harrick plasma, UK). Immediately after sealing, a 0.1% (g/mL) bovine gelatin (Gelatin from bovine skin, Sigma-Aldrich) coating was added to the microfluidic devices aimed at promoting cell adhesion, and the devices were stored at 4°C until cell seeding.

A surface pre-treatment using Trichloro(1H,1H,2H,2H-perfluorooctyl)silane (PFOCTS) (UTC Specialties, T2492-KG) by vapor deposition was applied to the master mold to facilitate the detachment of the PDMS layer from the wafer.

Cell lines and cell culture conditions

The experimental procedure involves two cancerous cell lines with metastatic potential. A549 cells are an established commercial lung cancer cell line[57] (a generous gift from Isabel Marzo Rubio), while PACA cells were derived directly from the metastatic neuroblastoma of a patient (generously provided by Jaime Font de Mora). Both cell types were transfected with a plasmid encoding the H2B-GFP fusion protein from Geoff Wahl (Addgene plasmid #11680) to generate a stable cell line constitutively expressing human histone H2B, one of the core proteins in DNA packaging, tagged with Green Fluorescent Protein (GFP). According to the laboratory of Geoff Wahl[39], the fluorescence intensity depends on the chromosome condensation state, and it does not affect the cell cycle progression, therefore, being a valuable tool for high-resolution imaging of DNA arrangement in real time in living cells[39].

The two cell lines were grown in Dulbecco's Modified Eagle Medium high in glucose (DMEM with 4.5 g/L D-Glucose, Gibco) supplemented with 10% Fetal Bovine Serum (FBS, Gibco) and 1% penicillin-streptomycin (antibiotic-antimycotic, Gibco). Cell cultures were incubated at 37 °C, 95% humidity, and 5% CO_2 conditions.

Cell lines were proven infection-free through PCR detection for mycoplasma, performed with specific probes Myc A (5' GGCGAATGGGTGAGTAACACG 3') and Myc B (5' CGGATAACGCTTGCGACCTATG 3') using a real-time PCR thermocycler (Bio Rad: CFX96 Real Time System) and visualized with gel imaging system (Bio Rad: ChemiDoc XRS + with Image Lab Software).

Cell seeding and high-resolution real-time in vitro experimental procedure

For cell seeding into the microfluidic devices, the cells are detached, resuspended in FBS-free medium, and then filtered through a 40 μm cell strainer to prevent cell aggregates.

First, 16.8 μL of FBS-free medium are loaded in the medium inlet and, immediately after, 50 μL of the cell stock solution were added to the cell inlet (see ports notation in Fig. 1b). Subsequently, 16.8 μL from the cell inlet were transferred to the adjacent loading port (the cell outlet) in order to reduce the flow and established the proper pressure to promote cell attachment at the entries of the channels. Note that these loading volumes were estimated through a fluid dynamics simulation in COMSOL Multiphysics using a simplified geometry consisting of straight confining microchannels. The differences between the geometries were not relevant for the calculations of the loading volumes, and they could be directly implemented in these devices.

Once a sufficient number of cells have adhered to the microchannels, the flow is halted by gradually transferring small volumes from the cell inlet to the cell outlet until equilibrium is reached. Thereafter, the microfluidic device was incubated for half an hour at 37 °C in a humid atmosphere and 5% CO_2 conditions. Following the incubation period, the six loading ports are emptied, and the two cell inlet/outlet ports are filled with FBS-free medium, whereas the four remaining ports on the opposite side are loaded with 20% FBS-enriched medium. This setup generates a chemoattractant gradient to favor cell migration through the microchannels.

Cell migration was monitored and recorded with time-lapse live microscopy using an inverted fluorescence optical microscope (Zeiss Axio Observer). To attain single-cell precision and high spatial resolution, particularly relevant for the analysis of the fluorescence intensity profile, a 63x oil immersion objective was employed.

The recording duration ranged from 20 to 24 hours for each experiment, with a time lapse interval of 10 minutes. It was conducted using two imaging channels, brightfield and EGFP, to capture the nucleus fluorescence signal. The parameters for the latter channel were adjusted to 10% for the light source intensity and 50 ms for the exposure time to minimize the risk of DNA damage and photobleaching. Cell viability was preserved throughout the experiment by implementing a cell incubation chamber in the microscope, which maintained regular culture conditions.

Imaging post-processing and nuclei segmentation

Raw microscope image data were processed using ImageJ through a custom-made macro to segment the fluorescent cell nuclei individually. Briefly, the macro implements a first segmentation stage in which a rough mask is generated through automatic thresholding to crop each nucleus from the original image and estimate its approximate location within the frame. In the second segmentation step, each image for the individual nuclei undergoes an edge detection method to adjust the mask to the nuclei contour. Once the segmentation was accomplished, the intensity histogram and morphological parameters, including the nuclei area, perimeter, major and minor axis, center of mass, etc., were measured and stored in a CSV file.

Subsequently, using MATLAB software, a drift correction algorithm was applied to align the frames with the horizontal axis of the image. Following successful alignment, a cell tracking code was developed to identify the nuclei path across the imaging sequence and to determine the state of the cell nuclei, confined or non-confined. For the analysis, three different zones were distinguished in the microchannels (see Fig. 3a), non-confining regions, confining regions, and a transition zone in between the former two, in which the results are not considered for the cell population analysis. Although nuclear envelope rupture plays a relevant role during confined migration[58], the constriction sizes in our experiments maintained nuclear integrity[43], resulting in rare rupture events. Cells with compromised nuclear envelopes, identified by cytoplasmic GFP and nuclear blebs, were excluded from analysis. It is also noteworthy that to prevent considering chromatin condensation effects attributed to mitosis while avoiding the use of cell-cycle control treatments that might interfere with native chromatin dynamics, we excluded from the analysis 20 frames (200 minutes) before and after cell division.

Segmentation of highly-condensed chromatin regions and quantification of chromatin cluster distribution

A segmentation algorithm was developed in MATLAB to identify regions with elevated fluorescence intensity, indicative of more condensed chromatin states. First, we apply a pixel intensity normalization over the original image to account for biological variation in H2B-GFP expression across different nuclei. This normalization was introduced by Eshghi et al.[35], it defines the normalized intensity for each pixel as

$$I_{norm} = \frac{I - I_{min}}{I_{mean}} \tag{1}$$

where I represents the original intensity of the pixel, I_{min} the minimum non-zero intensity in the frame, and I_{mean} the average intensity of the frame.

Finally, a custom MATLAB script implementing an adaptive image filter was used to compute the thresholds for the binary mask that identifies highly-condensed chromatin regions. This algorithm excludes pixels with intensities lower than 0.6 (normalized intensity), and it relies on the MATLAB function `adaptthresh` to select specific thresholds for the segmentation according to local mean intensity in neighboring pixels. Similar segmentation algorithms using this MATLAB function have already been described in the literature[59–61].

The evolution of these chromatin clusters over time is then addressed through histograms representing the distribution of cluster areas and the total number of clusters per nucleus among the cell population. We generated region-specific histograms that aggregate the relative area across all chromatin clusters (cluster area over total nucleus area), or the number of clusters, within each cell nucleus appearing in every temporal frame where the nucleus center lies within the specific microchannel region. Data from each cell were resampled to 100 points to avoid biasing the analysis against cells migrating faster in the microchannels. Note that the distributions are normalized with the total number of counts to represent the probability for cluster size or cluster number. Subsequently, the differences among the distributions for each region were quantified using Wasserstein distances, which indicate how similar two probability distributions are, such that smaller distance values correspond to more resembling distributions. This pairwise comparison was implemented in MATLAB based on the code published by Kolbe[48].

In addition, a population analysis of the distance between the center of mass of the nucleus and its geometric center (centroid) was performed to estimate the location where chromatin clusters preferentially accumulate.

The center of mass corresponds to the intensity-weighted centroid of the nucleus, i.e., the point representing the average position of the fluorescence signal across all pixels. It represents the coordinates where the intensity would accumulate if the signal were treated like physical mass. Formally, for an image where each pixel (x, y) has an intensity value $I(x, y)$:

$$x_{CM} = \frac{\sum(x \cdot I(x,y))}{\sum I(x,y)},\ y_{CM} = \frac{\sum(y \cdot I(x,y))}{\sum I(x,y)} \tag{2}$$

The geometric center is calculated as the arithmetic mean position of all the pixels in the nucleus. It consists of adding the pixels x-coordinates and dividing by the number of pixels to get the centroid x-coordinate, and accordingly for the centroid y-coordinate:

$$x_{centroid} = \frac{1}{n}\sum_{i=1}^{n} x_i,\ y_{centroid} = \frac{1}{n}\sum_{i=1}^{n} y_i \tag{3}$$

Then, we subtracted the centroid from the center of mass in y-coordinates, which aligns with the direction of the microchannels. Therefore, a positive value implies chromatin accumulation at the front of the cell while a negative value indicates chromatin accumulation at the rear of the cell.

Immunofluorescence assay targeting specific heterochromatin markers

To relate global chromatin condensation to heterochromatin content within the cell nucleus, we performed an immunofluorescence assay for heterochromatin marks H3K9me^3 and H3K27me^3, which target specifically heterochromatin regions, characterized by increased histone methylation.

Trimethylation of lysine 9 on histone H3 (H3K9me^3) is associated with constitutive heterochromatin, which is mostly located in centromeric and telomeric DNA regions, while trimethylation of lysine 27 on histone H3 (H3K27me^3) is associated with facultative heterochromatin, which is developmentally regulated.

Following the 24-hour period of cell confined migration in microfluidic devices under in vivo microscopy, cells in the devices were fixed using 4% paraformaldehyde (Sigma-Aldrich) to preserve cellular structures and then permeabilized with Triton X-100 (Sigma-Aldrich) to allow antibody penetration. To minimize non-specific binding, cells are incubated with a 0.5% BSA blocking buffer. Subsequently, we incubated the microfluidic device overnight with the two primary antibodies specific against different heterochromatin markers: Anti-Histone H3 (tri methyl K9) antibody (ab8898, Abcam) and Anti-Histone H3 (tri methyl K27) antibody (ab6002, Abcam). Finally, two fluorophore-conjugated secondary antibodies (goat anti-mouse Alexa Fluor 405 and donkey anti-rabbit Alexa Fluor 647)(1:200) were used to recognize each primary antibody, and confocal imaging (Confocal Microscopy STELLARIS 5 DLS, Leica Microsystems CMS, Germany) was performed to read the fluorescence signal. Heterochromatin content and distribution were analyzed using ImageJ to segment individual nuclei and, then, MATLAB to quantify fluorescence intensity among other parameters of interest. To measure the spatial correlation of heterochromatin markers and GFP signal, the MATLAB function `corr2` was implemented. This function is based on Pearson's correlation coefficient applied to all the elements in the array defining the nucleus fluorescence image. Note that, to compute the spatial correlation coefficient, the background of the images is considered a perfect match in the correlation function; therefore, an important fraction of the high correlation coefficient might be due to the background noise. To estimate the contribution of the background in the final computation, we tested two images of the same sample nucleus, but each containing a random distribution of intensity values within the nucleus contour. The correlation coefficient turned out to

be around 0.5, which was considered when evaluating the results for the immunofluorescent analysis.

Statistics and reproducibility

The statistical analysis was conducted using GraphPad Prism software v8.0.1. Two to four different experiments were performed and analyzed for each cell line following the experimental protocol developed. Cells were classified according to the confining microchannel through which they migrate, either a long or a short channel. For the PACA-H2B-GFP cell line, the sample size in long channels was $n = 71$, and in short channels it was $n = 65$. For the A549-H2B-GFP cell line, sample sizes were $n = 26$ and $n = 42$, respectively. Each experiment was evaluated separately, consistently yielding the same conclusions. The data were then combined for collective analysis and representation. Furthermore, reproducibility was confirmed between the two different cell lines.

First of all, the ROUT method was used to identify and exclude outliers from the data set before any further statistical analysis. For data following a normal distribution, a parametric one-way analysis of variance (ANOVA) with Tukey's multiple comparison test (two-sided test), was performed. Otherwise, in the absence of normality, a non-parametric Kruskal-Wallis test with Dunn's post hoc test for multiple comparisons (two-sided test) was designated. Statistical significance was defined as a p-value below 0.05, and results were reported according to APA guidelines: $p > 0.5$ (ns), $p < 0.05$ (*), $p < 0.01$ (**), $p < 0.001$ (***).

Polymeric model of chromatin

Polymer models of chromatin are a suitable representation of chromatin mesoscopic structure at the level of the experimental resolution. Our aim is, by means of numerical simulations, to correlate the experimental observations to a reorganization of chromatin as the nucleus translocates through a microfluidic confining channel. To this end, we propose a polymer model of chromatin that we will investigate through numerical simulations, an approach that has been successful in previous chromatin studies[62–65]. This model, adapted from[52], describes chromatin as a coarse grained beads-and-springs copolymer chain composed by N particles, each corresponding to ~50,000 base-pairs (50 kbp), of two types (representing heterochromatin and euchromatin) confined within a shell that models the nuclear envelope (see Fig. 6a). We chose a density for the chromatin fiber of $\rho = 0.2$, well within the physiological range[62]. The simulation particles (each representing approximately 250 nucleosomes, which we will refer to as beads from now on) are linked by harmonic springs[66,67] (corresponding to chromatin fiber), and heterochromatin and euchromatin domains are arranged along the chain following an exponential length distribution, with an average domain size of 64 beads, maintaining an overall 50/50 composition of both chromatin types. This proportion was chosen both as a simplification and to be able to observe large enough clusters in our simulation, given that only heterochromatin forms condensates.

The remaining interactions in the system are governed by a Wang-Frenkel potential[68], which accounts for steric repulsion between beads, as well as between beads and the confining shell. Additionally, in the case of heterochromatin, this potential includes attractive interactions among heterochromatin beads and, optionally, between heterochromatin and the nuclear lamina[24,64,69] (see Fig. 6). For a more detailed description of the interactions, see the Supplementary Note 1. Although most of the results are given for lamina-free interaction, simulations considering lamina interaction are included in the Supplementary Information for comparison (Supplementary Fig. 12).

Importantly, the confining shell deforms dynamically over time to mimic the experimental conditions, changing from a disk to a peanut-shaped geometry of constant height as it passes through a narrow confinement, and returning to a disk shape at the end of the simulation (see Fig. 6b). The definition of the geometry of the shell, along with its parameters, is included in the Supplementary Note 1 (Supplementary Fig. 9).

Reporting summary

Further information on research design is available in the Nature Portfolio Reporting Summary linked to this article.

Data availability

The data that support the findings of this study are openly available in Figshare[70]. The source data underlying the figures in this work are provided in Supplementary Data 2. Any other data is available from the corresponding authors on reasonable request.

Code availability

The segmentation algorithm used to process fluorescent microscope images is available on GitHub (https://github.com/yablazro/Segmentation-chromatin-clusters) and Zenodo[71]. Any other code is available from the corresponding authors on reasonable request.

Received: 22 July 2025; Accepted: 22 January 2026;
Published online: 06 February 2026

References

1. Irianto, J. et al. Nuclear constriction segregates mobile nuclear proteins away from chromatin. *Mol. Biol. Cell* **27** (2016).
2. Merino-Casallo, F., Gomez-Benito, M. J., Hervas-Raluy, S. & Garcia-Aznar, J. M. Unravelling cell migration: defining movement from the cell surface. *Cell Adhes. Migr.* **16**, 25–64 (2022).
3. Juste-Lanas, Y. et al. Confined cell migration and asymmetric hydraulic environments to evaluate the metastatic potential of cancer cells. *J. Biomech. Eng.* **144**, 074502 (2022).
4. Lambert, A. W., Pattabiraman, D. R. & Weinberg, R. A. Emerging biological principles of metastasis. *Cell* **168**, 670–691 (2017).
5. Paul, C. D. et al. Interplay of the physical microenvironment, contact guidance, and intracellular signaling in cell decision making. *FASEB J. : Off. Publ. Federation Am. Societies Exp. Biol.* **30**, 2161–2170 (2016).
6. Wolf, K. et al. Collagen-based cell migration models in vitro and in vivo. *Semin. cell developmental Biol.* **20**, 931–941 (2009).
7. Danielsson, B. E. et al. Chromatin condensation regulates endothelial cell adaptation to shear stress. *MBoC* **33**, ar101 (2022).
8. Rabineau, M. et al. Chromatin de-condensation by switching substrate elasticity. *Sci. Rep.* **8**, 12655 (2018).
9. Leclech, C. et al. Micro-scale topography triggers dynamic 3d nuclear deformations. *Advanced Science***12** (2025).
10. Mitra, A. et al. Acute chromatin decompaction stiffens the nucleus as revealed by nanopillar-induced nuclear deformation in cells. *Proc. Natl. Acad. Sci. USA* **122**, e2416659122 (2025).
11. Nava, M. M. et al. Heterochromatin-driven nuclear softening protects the genome against mechanical stress-induced damage. *Cell* **181**, 800–817.e22 (2020).
12. Heo, S.-J. et al. Biophysical regulation of chromatin architecture instills a mechanical memory in mesenchymal stem cells. *Sci. Rep.* **5**, 16895 (2015).
13. Damodaran, K. et al. Compressive force induces reversible chromatin condensation and cell geometry-dependent transcriptional response. *Mol. Biol. cell* **29**, 3039–3051 (2018).
14. Booth-Gauthier, E. A., Alcoser, T. A., Yang, G. & Dahl, K. N. Force-induced changes in subnuclear movement and rheology. *Biophys. J.* **103**, 2423–2431 (2012).
15. Thomas, C. H., Collier, J. H., Sfeir, C. S. & Healy, K. E. Engineering gene expression and protein synthesis by modulation of nuclear shape. *Proc. Natl. Acad. Sci.* **99**, 1972–1977 (2002).
16. Kalukula, Y., Stephens, A. D., Lammerding, J. & Gabriele, S. Mechanics and functional consequences of nuclear deformations. *Nat. Rev. Mol. cell Biol.* **23**, 583–602 (2022).
17. Tajik, A. et al. Transcription upregulation via force-induced direct stretching of chromatin. *Nat. Mater.* **15**, 1287–1296 (2016).

18. Zhao, J. Z., Xia, J. & Brangwynne, C. P. Chromatin compaction during confined cell migration induces and reshapes nuclear condensates. *Nat. Commun.* **15**, 9964 (2024).
19. Miroshnikova, Y. A., Nava, M. M. & Wickström, S. A. Emerging roles of mechanical forces in chromatin regulation. *J. cell Sci.* **130**, 2243–2250 (2017).
20. Martin, R. M. & Cardoso, M. C. Chromatin condensation modulates access and binding of nuclear proteins. *FASEB J.* **24**, 1066–1072 (2010).
21. Gerlitz, G. The emerging roles of heterochromatin in cell migration. *Front. Cell Dev. Biol.* **8**, 394 (2020).
22. Erdel, F. Phase transitions in heterochromatin organization. *Curr. Opin. Struct. Biol.* **80**, 102597 (2023).
23. Brangwynne, C. P., Tompa, P. & Pappu, R. V. Polymer physics of intracellular phase transitions. *Nat. Phys.* **11**, 899–904 (2015).
24. Adame-Arana, O., Bajpai, G., Lorber, D., Volk, T. & Safran, S. Regulation of chromatin microphase separation by binding of protein complexes. *Elife* **12**, e82983 (2023).
25. Eshghi, I., Zidovska, A. & Grosberg, A. Y. Activity-driven phase transition causes coherent flows of chromatin. *Phys. Rev. Lett.* **131**, 048401 (2023).
26. Kant, A. et al. Active transcription and epigenetic reactions synergistically regulate meso-scale genomic organization. *Nat. Commun.* **15**, 4338 (2024).
27. Stephens, A. D., Banigan, E. J., Adam, S. A., Goldman, R. D. & Marko, J. F. Chromatin and lamin a determine two different mechanical response regimes of the cell nucleus. *Mol. Biol. cell* **28**, 1984–1996 (2017).
28. Lammerding, J., Engler, A. J. & Kamm, R. Mechanobiology of the cell nucleus. *APL Bioeng.* **6**, 040401 (2022).
29. Scott, A. K., Rafuse, M. & Neu, C. P. Mechanically induced alterations in chromatin architecture guide the balance between cell plasticity and mechanical memory. *Front. cell developmental Biol.* **11**, 1084759 (2023).
30. Hsia, C.-R. et al. Confined migration induces heterochromatin formation and alters chromatin accessibility. *iScience***25** (2022).
31. Hovet, O. et al. Nuclear mechano-confinement induces geometry-dependent hp1alpha condensate alterations. *Commun. Biol.* **8**, 308 (2025).
32. Hannezo, E. & Heisenberg, C.-P. Mechanochemical feedback loops in development and disease. *Cell* **178**, 12–25 (2019).
33. De Corato, M. & Gomez-Benito, M. J. Interplay of chromatin organization and mechanics of the cell nucleus. *Biophys. J.* (2024).
34. Pagliara, S. et al. Auxetic nuclei in embryonic stem cells exiting pluripotency. *Nat. Mater.* **13**, 638–644 (2014).
35. Eshghi, I., Eaton, J. A. & Zidovska, A. Interphase chromatin undergoes a local sol-gel transition upon cell differentiation. *Phys. Rev. Lett.* **126**, 228101 (2021).
36. Stephens, A. D. et al. Chromatin histone modifications and rigidity affect nuclear morphology independent of lamins. *MBoC* **29**, 220–233 (2018).
37. Gerlitz, G. & Bustin, M. Efficient cell migration requires global chromatin condensation. *J. Cell Sci.* **123**, 2207–2217 (2010).
38. Liu, S. et al. Mechanotherapy in oncology: Targeting nuclear mechanics and mechanotransduction. *Adv. Drug Deliv. Rev.* **194**, 114722 (2023).
39. Kanda, T., Sullivan, K. F. & Wahl, G. M. Histone–gfp fusion protein enables sensitive analysis of chromosome dynamics in living mammalian cells. *Curr. Biol.* **8**, 377–385 (1998).
40. Chen, M. B., Whisler, J. A., Jeon, J. S. & Kamm, R. D. Mechanisms of tumor cell extravasation in an in vitro microvascular network platform. *Integr. Biol. : Quant. Biosci. nano macro* **5**, 1262–1271 (2013).
41. Stöberl, S. et al. Nuclear deformation and dynamics of migrating cells in 3d confinement reveal adaptation of pulling and pushing forces. *Sci. Adv.* **10**, eadm9195 (2024).
42. Mouelhi, M. et al. Mitosis sets nuclear homeostasis of cancer cells under confinement (2024).
43. Bastianello, G. et al. Mechanical stress during confined migration causes aberrant mitoses and c-myc amplification. *Proc. Natl. Acad. Sci. USA* **121**, e2404551121 (2024).
44. Dahl, K. N., Engler, A. J., Pajerowski, J. D. & Discher, D. E. Power-law rheology of isolated nuclei with deformation mapping of nuclear substructures. *Biophys. J.* **89**, 2855–2864 (2005).
45. Lee, D. S. et al. Size distributions of intracellular condensates reflect competition between coalescence and nucleation. *Nat. Phys.* **19**, 586–596 (2023).
46. Brangwynne, C. P., Mitchison, T. J. & Hyman, A. A. Active liquid-like behavior of nucleoli determines their size and shape in xenopus laevis oocytes. *Proc. Natl. Acad. Sci.* **108**, 4334–4339 (2011).
47. Arsenadze, G. et al. Anomalous coarsening of coalescing nucleoli in human cells. *Biophys. J.* **123**, 1467–1480 (2024).
48. Kolbe, N. nklb/wasserstein-distance: v1.0. https://doi.org/10.5281/zenodo.10912241 Version v1.0 (2024).
49. Davidson, P. M. et al. Nesprin-2 accumulates at the front of the nucleus during confined cell migration. *EMBO Rep.* **21**, e49910 (2020).
50. Bos, I. et al. The mechanism of nesprin-2 accumulation at the nucleus front during confined cell migration. *Biophysical J.* **124**, 2056–2069 (2025).
51. Nicodemi, M. & Pombo, A. Models of chromosome structure. *Curr. Opin. cell Biol.* **28**, 90–95 (2014).
52. Bajpai, G., Amiad Pavlov, D., Lorber, D., Volk, T. & Safran, S. Mesoscale phase separation of chromatin in the nucleus. *eLife* **10**, e63976 (2021).
53. Tong, Z. et al. Chemotaxis of cell populations through confined spaces at single-cell resolution. *PloS one* **7**, e29211 (2012).
54. Davidson, P., Sliz, J., Isermann, P., Denais, C. & Lammerding, J. Design of a microfluidic device to quantify dynamic intra-nuclear deformation during cell migration through confining environments. *Integrative biology: quantitative biosciences from nano to macro* **7** (2015).
55. Zhang-Zhou, J. et al. Car-t cells are more affected than t lymphocytes by mechanical constraints: A microfluidic-based approach. *Life Sci.* **363**, 123335 (2025).
56. Shin, Y. et al. Microfluidic assay for simultaneous culture of multiple cell types on surfaces or within hydrogels. *Nat. Protoc.* **7**, 1247–1259 (2012).
57. Giard, D. J. et al. In vitro cultivation of human tumors: establishment of cell lines derived from a series of solid tumors. *J. Natl. Cancer Inst.* **51**, 1417–1423 (1973).
58. Denais, C. M. et al. Nuclear envelope rupture and repair during cancer cell migration. *Science* **352**, 353–358 (2016).
59. Karrobi, K. et al. Fluorescence lifetime imaging microscopy (flim) reveals spatial-metabolic changes in 3d breast cancer spheroids. *Sci. Rep.* **13**, 3624 (2023).
60. Heinrich, S. et al. Glucose stress causes mrna retention in nuclear nab2 condensates. *Cell Rep.* **43**, 113593 (2024).
61. Zonca, L. et al. Unveiling the functional connectivity of astrocytic networks with astronet, a graph reconstruction algorithm coupled to image processing. *Commun. Biol.* **8**, 114 (2025).
62. Halverson, J. D., Smrek, J., Kremer, K. & Grosberg, A. Y. From a melt of rings to chromosome territories: the role of topological constraints in genome folding. *Rep. Prog. Phys.* **77**, 022601 (2014).
63. Amiad-Pavlov, D. et al. Live imaging of chromatin distribution reveals novel principles of nuclear architecture and chromatin compartmentalization. *Sci. Adv.* **7**, eabf6251 (2021).
64. Falk, M. et al. Heterochromatin drives compartmentalization of inverted and conventional nuclei. *Nature* **570**, 395–399 (2019).
65. Rosa, A. & Everaers, R. Structure and dynamics of interphase chromosomes. *PLoS Comput. Biol.* **4**, e1000153 (2008).

66. Bajpai, G. & Safran, S. Mesoscale, long-time mixing of chromosomes and its connection to polymer dynamics. *PLOS Comput. Biol.* **19**, 1–30 (2023).
67. Amitai, A. & Holcman, D. Polymer physics of nuclear organization and function. *Phys. Rep.* **678**, 1–83 (2017).
68. Wang, X., Ramírez-Hinestrosa, S., Dobnikar, J. & Frenkel, D. The Lennard-Jones potential: when (not) to use it. *Phys. Chem. Chem. Phys.* **22**, 10624–10633 (2020).
69. Câmara, A. S. & Mascher, M. Consistencies and contradictions in different polymer models of chromatin architecture. *Comput. Struct. Biotechnol. J.* **21**, 1084–1091 (2023).
70. Blazquez-Romero, M. d. V. Dataset manuscript: "periodic confined cell migration drives partially reversible chromatin reorganization", Blazquez-Romero et al. https://doi.org/10.6084/m9.figshare.30657911 (2025).
71. Blazquez-Romero, M. d. V. Segmentation of chromatin clusters https://doi.org/10.5281/zenodo.18145272 (2026).

Acknowledgements

This work was supported by MCIN/AEI/10.13039/501100011033 and ERDF A way of making Europe through grants PID2024-155426OB-I00 (MJG-B), PID2022-139803NB-I00 (MDC), PID2023-147734NB-I00 (FF, AS-A), PID2023-147067NB-I00 (MM-C), FPI fellowships PRE2023-001133 (MM-C) and PRE2021-100456 (AS-A), the Ramon y Cajal fellowship RYC2021-030948-I, also funded by the EU under the NextGeneration EU/PRTR program (MVB-R, MDC); by the Aragon autonomous region government through the research grant LMP21 (MVB-R, MSM, MDC, MJG-B) and the research group support of E36_23R FENOL (FF, AS-A), T50_23R M2BE (MJG-B, MVB-R) and TFD (MDC); and by European Research Council (ERC) under the European Union's Horizon2020 research and innovation programme (ICoMICS GA101018587) (MJG-B). Also, ASPANOA and Aragon Institute for Engineering Research (MVB-R). Thanks to Isabel Marzo Rubio and Jaime Font de Mora for generously providing the cell lines used in this work. Special thanks to Jack Zhang-Zhou, whose expertise and instruction in the laboratory technique were instrumental to this project.

Author contributions

M.V.B.-R. did the investigation, data curation, visualization, and writing of the original draft. M.V.B.-R. and M.S. optimized the experimental protocol and worked on the software for image data processing codes. M.V.B.-R., M.D.C., and M.J.G.-B. worked on the methodology and formal analysis. M.M.-C., A.S.-A., and F.F. worked on the development, implementation, simulation, and writing of the coarse-grained polymer chromatin computational model. M.V.B.-R., M.M.-C., A.S.-A., F.F., M.D.C., and M.J.G.-B. participated in review and editing. M.D.C. and M.J.G.-B. conceptualized the study, found resources, supervised, and administered the project. M.D.C. and M.J.G.-B. acquired the funding for this work.

Competing interests

The authors declare no competing interests.

Additional information

Supplementary information The online version contains supplementary material available at https://doi.org/10.1038/s42003-026-09637-4.

Correspondence and requests for materials should be addressed to Marco De Corato or Maria Jose Gomez-Benito.

Peer review information *Communications Biology* thanks Paulina Nastaly and the other anonymous reviewers for their contribution to the peer review of this work. Primary Handling Editors: Manuel Breuer and George Inglis. A peer review file is available.